Journal of Materials Chemistry C

ROYAL SOCIETY OF CHEMISTRY

PAPER

View Article Online
View Journal

Cite this: DOI: 10.1039/d5tc03655k

Enhanced deep-blue emission and quantum yield of $Ca_{0.995}YGaO_4$:0.5%Bi^{3+} *via* lithium-based flux additives

Abdelrhman Yousif, *[ab] Andrey Turshatov, *[a] Dmitry Busko,[a] Krishnan Rajagopalan,[a] Elizabeth Coetsee-Hugo [c] and Bryce S. Richards *[ad]

In this work, Bi^{3+}-doped $CaYGaO_4$ phosphors were synthesised through solid-state reaction and systematically optimised using lithium-based fluxes to enhance their photoluminescence quantum yield (PLQY) in the blue region. Comparative studies between Li_2O and Li_2CO_3 fluxes revealed distinct structural and optical impacts. Rietveld refinement confirmed effective Bi^{3+} incorporation, with samples treated using 2% Li_2CO_3 and 1% Li_2O exhibiting superior crystallinity. SEM analysis showed molten-like particle morphologies and increased porosity in Li_2CO_3-treated samples features absent in those treated with Li_2O. XPS results highlighted a notable reduction in oxygen-related defects in Li_2CO_3-modified phosphors, correlating with improved PLQY performance. Photoluminescence measurements demonstrated strong blue emission at 430 nm under 330 nm excitation, alongside additional red (720 nm) and near-infrared (780 nm) emissions from stabilised Bi^{2+} species, attributed to lithium-induced lattice rearrangements. The sample treated with Li_2CO_3 achieved a PLQY of 70%, surpassing flux-free and Li_2O-assisted counterparts, reinforcing the pivotal role of flux chemistry in fine-tuning emission efficiency. In particular, lithium carbonate flux profoundly influences Bi^{3+}-doped $CaYGaO_4$ phosphors, establishing flux chemistry as a versatile tool for engineering efficient blue emitters for photonic applications.

Received 9th October 2025,
Accepted 29th March 2026

DOI: 10.1039/d5tc03655k

rsc.li/materials-c

1. Introduction

Blue-emitting phosphors within the 400–500 nm spectral range are vital to emerging light-conversion technologies. They serve as key components in solid-state lighting, ultra-high-resolution displays, and optical communication systems.[1–3] Additionally, their spectral flexibility enables applications in agricultural photonics, where specific wavelengths enhance plant growth.[1,4,5] The photosynthetically active radiation (PAR) spectrum of the majority of plants exhibits peaks in the blue and red wavelengths.[6] Significant research has been conducted on luminescent materials that absorb the underutilised ultraviolet (UV) light and emit this in the red[7] or far-red,[8] however less research has been conducted on high photoluminescence quantum yield (PLQY) UV-absorbing blue-emitting materials.

Recent studies have also highlighted alternative blue-emitting candidates including Bi^{3+}-doped halide nanocrystals,[9] Cd-based coordination complexes,[10] nitrogen-doped carbon dots, and organic dyes such as violanthone derivatives that offer promising PLQY and spectral tunability,[11] yet remain underrepresented in current reviews.

This study focuses on Bi^{3+}-doped phosphors due to their favourable combination of high PLQY, robust thermal and chemical stability, emission wavelengths that closely align with the blue peak of the PAR spectrum, and relatively low toxicity compared to other heavy-metal-based emitters; while factors such as particle size and mixed-valence behaviour remain complex, they offer additional avenues for tuning luminescent performance.

Bi^{3+}-activated oxide hosts stand out among the underexplored materials due to their broad emission profiles and strong near-UV absorption.[2,12] These properties stem from the adaptable $6s^2$ electronic configuration of Bi^{3+} ions,[3] which allows transitions from the $^1S_0$ ground state to excited $^3P_0$, $^3P_1$, $^3P_2$, and $^1P_1$ levels. The dipole-allowed $^1S_0 \rightarrow {}^3P_1$ transition predominantly drives intense blue luminescence.[2,13]

$CaYGaO_4$ doped with Bi^{3+} has garnered considerable interest as a versatile luminescent material, distinguished by its pronounced absorption in the near-UV region and efficient blue

[a] Institute of Microstructure Technology, Karlsruhe Institute of Technology (KIT), Hermann-von-Helmholtz-Platz 1, 76344 Eggenstein-Leopoldshafen, Germany. E-mail: abdelrhman.mohmmed@kit.edu
[b] Department of Physics, Faculty of Education, University of Khartoum, P.O. Box 321, Omdurman 11115, Sudan. E-mail: abdelrhman.yousif@uofk.edu
[c] Department of Physics, University of the Free State, Bloemfontein ZA9300, South Africa
[d] Light Technology Institute, Karlsruhe Institute of Technology, Engesserstrasse 13, 76131 Karlsruhe, Germany

emission. These attributes enable its deployment in multiple photonic applications, including persistent luminescence in elevated temperature conditions,[14] energy transfer investigations within Bi^{3+}/Mn^{4+} (ref. 15) and Bi^{3+}/Tb^{3+} (ref. 16) co-doped systems, and spectral optimization for near-UV-pumped white-light-emitting diodes.[3]

Fu *et al.*[2] demonstrated that Bi^{3+}-activated $CaYGaO_4$ synthesised with partial Y^{3+} substitution and Li_2CO_3 flux exhibited a broad emission centred at 435 nm and a PLQY of 47.5%.[2] Considering the minimal difference in ionic radii between Ca^{2+} (1.00 Å) and Bi^{3+} (1.03 Å), it is plausible that Bi^{3+} may also occupy Ca^{2+} sites within the crystal lattice. Based on this assumption, the present study adopts a targeted substitution approach by introducing Bi^{3+} at a fixed concentration of 0.5%, yielding the $Ca_{0.995}YGaO_4$:0.5%Bi^{3+} phosphor. Unlike the approach taken by Fu *et al.*,[2] the present synthesis was performed under Ca^{2+} stoichiometric deficiency rather than Y^{3+} deficiency, offering new insight into site occupancy and its influence on luminescent behaviour.

In addition, this study also explores the emergence of Bi^{2+}-related luminescence in the far red as a secondary phenomenon, offering deeper insight into possible mixed-valence states and charge compensation mechanisms within the $Ca_{0.995}YGaO_4$:0.5%Bi^{3+} system.

Flux-assisted synthesis plays a critical role in optimizing crystallographic quality and luminescent behaviour, particularly in cases involving aliovalent substitution ($Bi^{3+} \rightarrow Ca^{2+}$). Lithium-based fluxes, *e.g.* Li_2CO_3, have demonstrated success in promoting phase purity and suppressing oxygen-related defects, thereby enhancing PLQY and overall emission performance.[2,17] The choice of flux agent is thus a key parameter in material synthesis.[18]

Lithium-based fluxes have not been widely employed in $CaYGaO_4$ and related layered gallates due to their volatility, pronounced chemical reactivity, and tendency to induce secondary phases or unpredictable defect states. However, recent studies by Fu *et al.*[2] demonstrate that, when carefully optimized, Li-based fluxes can significantly enhance crystallinity and reduce oxygen-related defects, thereby improving photoluminescence efficiency.

While Li_2CO_3 is widely adopted, Li_2O remains comparatively underexplored in the context of oxide phosphor development. Its distinct chemical properties may influence phase formation, particle morphology, and defect dynamics in ways not yet fully understood warranting further investigation into its role as an alternative flux.

Its inclusion may influence phase formation, particle morphology, and defect behaviour. Exploring the use of Li_2O as an alternative flux to Li_2CO_3 provides a valuable opportunity to enhance our understanding of flux chemistry and its impact on photophysical properties.

Although lithium flux–assisted enhancement of Bi^{3+} emission has been reported before, our work is novel in revealing that lithium fluxes not only improve crystallinity but also suppress oxygen-related defects, stabilize Bi^{3+}/Bi^{2+} coexistence, and promote Bi^{3+} substitution at Ca^{2+} sites, thereby unlocking dual emissions and record-high photoluminescence efficiency in $CaYGaO_4$.

Therefore, this work aims to determine whether $Ca_{0.995}YGaO_4$:0.5%Bi^{3+} phosphors synthesised using Li_2CO_3 and Li_2O exhibit distinct differences in crystal structure, PLQY, and emission intensity. Specifically, it examines how flux agents affect structural refinement, defect states, and particle morphology through charge compensation and substitution mechanisms. To this end, the samples were synthesised *via* a conventional solid-state reaction method. Their structural and optical properties were systematically investigated using X-ray diffraction (XRD) combined with Rietveld refinement, X-ray photoelectron spectroscopy (XPS), and scanning electron microscopy (SEM). Photoluminescence characterization, including measurements of the absolute PLQY, was also performed to evaluate the emission efficiency.

2. Materials and methods

2.1. Phosphor preparation

Two sets of $Ca_{0.995}YGaO_4$:0.5%Bi^{3+} phosphor materials were synthesised *via* a conventional high-temperature solid-state reaction method conducted under ambient air. Stoichiometric amounts of $CaCO_3$ (99.5%, Thermo Fisher Scientific), Y_2O_3 (99.99%, Chempur), Ga_2O_3 (99.99%, Chempur), and Bi_2O_3 (99.9%, Chempur) were precisely weighed and thoroughly homogenised using an agate mortar. For fluxing studies, lithium-containing compounds were introduced in two variations: (i) the first series utilised varying the wt% concentrations of Li_2CO_3 (99.995%, Chempur); (ii) the second series incorporated different amounts of wt% concentrations of Li_2O (99.5%, Thermo Fisher Scientific). The mixtures were pre-sintered at 600 °C for 5 hours to enable partial diffusion and interaction among precursors. Subsequently, the samples were cooled to room temperature, reground, and subjected to final sintering at 1300 °C for 5 hours to promote crystallization and densification. The resulting powders were finely ground and used for structural and optical characterization.

2.2. Phosphor characterization

The structural properties of $Ca_{0.995}YGaO_4$:0.5%Bi^{3+} phosphors were examined using XRD over a 2θ range of 15°–60°, recorded with a Bruker D8 DISCOVER diffractometer. Crystallographic structures were illustrated using the Diamond 5.1.0 build 49 software for visual modelling. Rietveld refinement of XRD data was conducted using the FullProf Suite, applying a pseudo-Voigt profile function, background correction, and preferred orientation modelling.

Surface morphology and particle size were analysed using SEM – Zeiss SUPRA 60VP system equipped with a secondary electron detector (SE-II). Prior to imaging, samples were sputter-coated with a thin gold layer to improve conductivity and minimise charging effects.

XPS measurements were performed using a PHI Quantes Scanning Dual X-ray Microprobe equipped with a monochromatic

Al K_α source ($h\nu$ = 1486.6 eV). Spectra were acquired under ultra-high vacuum conditions (base pressure: 8.4×10^{-10} Torr) with a pass energy of 26 eV, yielding a photoelectron energy resolution of $\leq$0.4 eV. The analysis focused on the O 1s core level to assess changes in oxygen-related defects and electronic environments. Peak fitting for excitation spectra and XPS data was performed using Origin 2023 software, applying a Gaussian function for spectral fitting.

Particle size distribution was measured using a Fritsch Analysette 22 NeXT Nano laser particle sizer, with a measurement range of 0.01 to 3800 μm.

The absolute PLQY was measured using a custom-built optical setup incorporating an integrating sphere (LabSphere Inc), similar to that described previously.[19] Samples were excited with low-power UV LEDs (325 nm and 365 nm, Roithner GmbH), and the emitted light was collected with a spectrometer (AvaSpec-ULS2048 × 64TEC-EVO, Avantes BV) *via* an optical fibre (BFY200MS02, Thorlabs Inc.). The PLQY system was irradiance-calibrated using a deuterium–halogen lamp (AvaLight DH-S, Avantes BV) and wavelength-calibrated with a Mercury–Argon calibration light source (HG-1, Ocean Optics). Samples were mounted in a quartz sheet holder (QGA33, Aireka Scientific) to avoid parasitic UV absorption. Data acquisition and spectral integration were semi-automated using a LabVIEW routine, and PLQY values were calculated following the DeMello procedure.[20] Replicate measurements were not performed; values are therefore reported as single calibrated determinations.

3. Results and discussion

3.1. Bi^{3+} substitution and ionic mismatch in $CaYGaO_4$

The substitution of Ca^{2+} by Bi^{3+} plays a critical role in determining the structural stability of the phosphor material. This substitution process is evaluated through the ionic radius mismatch parameter (D_r), which serves as an indicator of substitution feasibility and its impact on lattice distortion. The D_r value is calculated using the eqn (1) outlined in ref. 21, with ionic radii data obtained from ref. 22:

$$D_r = \frac{R_h(CN) - R_d(CN)}{R_h(CN)}, \quad (1)$$

where D_r, CN, R_h (CN), and R_d (CN) represent the percentage variation in ionic radii, the coordination number, the radius of the host cation, and the radius of the dopant ion, respectively.

Given the potential for Bi^{3+}, Bi^{2+}, and Li^+ to occupy various polyhedral sites within the $Ca_{0.995}YGaO_4$ lattice, substitutional feasibility was assessed for Ca^{2+}, Y^{3+}, and Ga^{3+} positions. As summarised in Table 1, substitutions at Ca^{2+} and Y^{3+} sites fall within the acceptable mismatch threshold ($D_r < 30\%$), indicating favourable lattice integration. In contrast, Ga^{3+} site substitutions exhibit excessive mismatch, suggesting likely lattice disruption. Li^+ ions similarly favour Ca^{2+} and Y^{3+} sites due to more compatible ionic radii.

For the charge-compensation mechanism in $CaYGaO_4$, substitution of Bi^{2+}/Bi^{3+} ions at Ca^{2+} sites introduce a charge imbalance that must be compensated to preserve electrostatic neutrality. Several compensation pathways have been reported in the literature (*e.g.*, Wang *et al.*[3] for $CaYGaO_4$; Puchalska *et al.*[23] for Bi substitution in $SrAl_4O_7$; Yousif *et al.* for Bi substitution in CaO[12]). The dominant mechanisms can be summarised as follows. Substitution of Bi^{3+} at Ca^{2+} sites generate a +1-excess charge, which may be compensated either by Ca vacancies $\left(3Ca_{Ca}^{\times} \rightarrow 2Bi_{Ca}^{\bullet} + V_{Ca}''\right)$ or by oxygen interstitials $\left(Bi_{Ca}^{\bullet} + O_i''\right)$. Bi^{3+} substitution at Y^{3+} sites are isovalent and therefore does not require charge compensation. In contrast, Bi^{2+} can replace Ca^{2+} directly in an isovalent manner, and the emergence of Bi^{2+}-related red/NIR emission in our samples supports the presence of such centres. The O 1s XPS analysis further shows that Li_2CO_3 suppresses vacancy-related oxygen species, indicating that Li^+ assists charge compensation and stabilises mixed Bi^{3+}/Bi^{2+} incorporation, consistent with the enhanced PLQY.

Although our present work is experimentally focused with a fixed Bi^{3+} doping concentration of 0.5%, previous density functional theory (DFT) studies have demonstrated that Bi^{3+}/Bi^{2+} site occupation and flux chemistry strongly influence band structure, band gap, and charge density Ogawa *et al.*,[24] Ahmed *et al.*[25] These reports provide theoretical precedent supporting our interpretation of flux-assisted site substitution and defect compensation.

Table 1 Ionic radius mismatch factor (D_r) analysis for cation substitution in $CaYGaO_4$. D_r values are calculated based on the ionic radii of host and dopant cations, considering their respective coordination numbers (CN). This analysis evaluates the substitutional compatibility of Bi^{3+}, Bi^{2+}, and Li^+ at Ca^{2+}, Y^{3+}, and Ga^{3+} sites within the $CaYGaO_4$ lattice. A D_r value below 30% indicates feasible lattice integration, whereas values exceeding 30% suggest potential structural distortion or instability

Host cation (CN) radii (Å)	Dopant (CN) radii (Å)	D_r (%)
Ca^{2+} (6) 1.00	Bi^{3+} (6) 1.03	3.0
	Bi^{2+} (6) 1.17	17
	Li^+ (6) 0.76	24
Y^{3+} (6) 0.90	Bi^{3+} (6) 1.03	14.4
	Bi^{2+} (6) 1.17	30
	Li^+ (6) 0.76	15
Ga^{3+} (4) 0.47	Bi^{3+} (4) 0.96	51
	Bi^{2+} (4) 1.31	101.5
	Li^+ (4) 0.73	55

3.2. XRD results

Fig. 1(a) and (b) present powder XRD patterns of $Ca_{0.995}YGaO_4$:0.5%Bi^{3+} phosphors synthesised using two different lithium-based fluxes: Li_2CO_3 and Li_2O, respectively. These patterns align closely with the standard reference for $CaYGaO_4$ (JCPDS card no. 81-0742), confirming formation of a single-phase material. The absence of secondary diffraction peaks further indicates high phase purity, even in the presence of lithium additives. No significant peak shifts are detected in the flux-free sample, likely due to the low and fixed Bi^{3+} doping level. However, increasing flux content introduces subtle peak

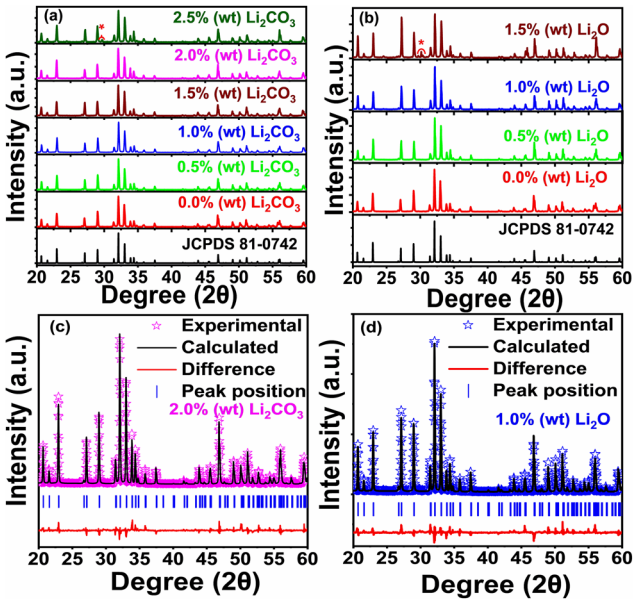

Fig. 1 Powder X-ray diffraction (XRD) patterns of $Ca_{0.995}YGaO_4$:0.5%Bi^{3+} phosphor materials synthesised using two lithium-based fluxes: (a) Li_2CO_3 and (b) Li_2O. Corresponding Rietveld refinement profiles are shown in (c) and (d), confirming phase purity and crystallographic fitting accuracy.

broadening – as shown in Fig. S1 and S2 in the SI – suggesting possible changes in crystallinity or the onset of lattice strain.

For Li_2CO_3-treated samples, the $CaYGaO_4$ phase persists up to 2.0 wt%. At 2.5 wt%, a new diffraction peak emerges near 29.6° marked with a red asterisk in Fig. 1(a) attributed to $CaCO_3$ based on ICSD PDF no. 01-070-0095 (see Fig. S1). This phase may be stabilised or modified by Bi^{2+} incorporation under CO_2-rich synthesis conditions, potentially contributing to deep red luminescence (see Luminescence section).

The Li_2O-treated samples displayed in Fig. 1(b) retain well-defined crystalline patterns at 0.5 wt% and 1.0 wt%. At higher Li_2O levels, diffraction peaks shift slightly toward higher 2θ angles, indicating possible Li^+ incorporation *via* interstitial sites or cation substitution in oxide phosphor hosts (lanthanum oxycarbonate,[17] rare-earth oxides such as Y_2O_3:Eu^{3+},[18] and related oxides[26]).

A distinct peak at 30.15° appears at 1.5 wt% Li_2O (marked with a red asterisk), matching ICSD PDF no. 121813, corresponding to the $(Ca_{12}Ga_{14}O_{33})_{1.667}$ phase (Fig. S3).

The divergence in secondary phase formation between Li_2CO_3 and Li_2O likely reflects their distinct chemical behaviour. Li_2CO_3 decomposes at higher temperatures than $CaCO_3$ and releases CO_2; however, due to its relatively low concentration and delayed decomposition onset, it is unlikely to significantly stabilise $CaCO_3$ during calcination. In contrast, Li_2O being carbonate-free and strongly basic favours oxygen-rich environments that promote the formation of complex oxides such as $(Ca_{12}Ga_{14}O_{33})_{1.667}$.

To further evaluate the crystal structure, Rietveld refinement was performed. Representative refinement profiles for 2.0 wt% Li_2CO_3 and 1.0 wt% Li_2O-treated samples are shown in Fig. 1(c) and (d), respectively. The models demonstrate excellent agreement between experimental and calculated patterns, confirming structural fidelity and phase purity. The extracted lattice parameters and reliability indices are provided in Table S1 of the SI.

The crystal structure of $CaYGaO_4$, is illustrated in Fig. 2, featuring three distinct cationic sites occupied by Ca^{2+}, Y^{3+}, and Ga^{3+}. The Ca^{2+} and Y^{3+} ions reside in separate octahedral environments (A1 and A2), while Ga^{3+} occupies tetrahedral A3 sites. The distorted CaO_6^{10-} octahedra form infinite edge-sharing chains along the *b*-axis, whereas corner-sharing YO_6^{9-} octahedra extend perpendicular to the *a*-axis, producing puckered layers. Interstitial GaO_4^{5-} tetrahedra fill voids between octahedra but remain spatially isolated, lacking direct connectivity. Energetically, low-valent cations like Ca^{2+} favour edge-sharing sites due to shorter A–A distances, minimizing Coulombic repulsion and stabilizing the lattice.[27] In contrast, smaller trivalent cations such as Y^{3+} are stabilised in corner-sharing environments, consistent with crystallographic ordering based on ionic radius and charge differentiation.[1,2]

3.3. Particle size distribution and morphology results

To investigate the effect of lithium flux on particle size, Fig. 3 presents volume-based cumulative particle size distribution curves $Q_3(x)$ and corresponding differential distributions $dQ_3(x)$ as a function of particle size x. These measurements were obtained for two representative samples: (i) the flux-free $Ca_{0.995}YGaO_4$:0.5%Bi^{3+}, and (ii) a Li_2CO_3-assisted counterpart ($Ca_{0.995}YGaO_4$:0.5%Bi^{3+}, 0.5 wt% Li_2CO_3). The flux-free sample exhibits a unimodal distribution in the 1–100 μm range, whereas the sample synthesised with Li_2CO_3 flux shows a bimodal distribution extending from 1–250 μm. This highlights the influence of fluxes on particle growth behaviour. Fig. S4 further illustrates particle size distribution for samples synthesised with Li_2O flux, revealing a distinct secondary population of larger particles. Similar phenomena have been reported by Han *et al.*,[28] who demonstrated that Li_2CO_3 flux alters particle size characteristics, resulting in bimodal morphology and improved crystallinity. This behaviour was attributed to flux role in modulating grain growth kinetics and facilitating particle coalescence during sintering. Additionally, their findings

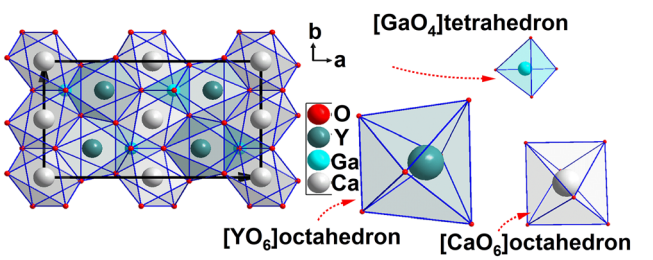

Fig. 2 The crystal structure of $CaYGaO_4$ adopts an olivine-type framework with orthorhombic symmetry (space group *Pnma*, no. 62). Ca^{2+} and Y^{3+} ions occupy octahedral sites, each coordinated by six oxygen atoms to form [CaO_6] and [YO_6] units, respectively. Ga^{3+} ions reside in tetrahedral sites, coordinated by four oxygen atoms to form [GaO_4] units.[1]

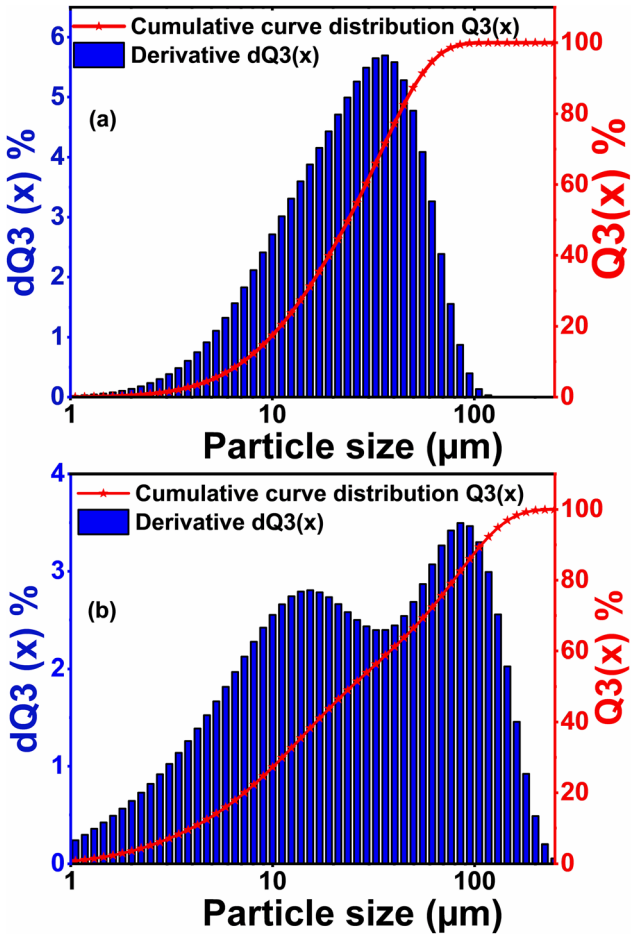

Fig. 3 Particle size distribution curves $Q_3(x)$ and their derivatives $dQ_3(x)$, plotted as a function of particle size x, for two samples: (a) $Ca_{0.995}YGaO_4$:0.5%Bi^{3+} and (b) $Ca_{0.995}YGaO_4$:0.5%Bi^{3+},0.5% Li_2CO_3. The derivative curves $dQ_3(x)$ indicate the rate of change in particle accumulation across size intervals, providing insight into grain growth behaviour influenced by lithium-based flux addition.

show that Li_2CO_3 effectively reduces agglomeration and promotes grain boundary fusion, thereby enhancing material homogeneity.

Fig. 4 presents SEM images of $Ca_{0.995}YGaO_4$:0.5%Bi^{3+} samples synthesised under flux-free conditions and with lithium-based flux treatments. The particle morphologies show a clear dependence on flux type, with mixtures of small and large irregular agglomerates exhibiting varied grain compactness and generally smooth surfaces. As indicated by blue markers, no pores or molten spherical particles are observed in flux-free samples. In contrast, soft, molten-like spherical particles and visible pores are evident in samples treated with Li_2CO_3 flux, suggesting distinct microstructural modifications. These features are absent in samples synthesised using Li_2O flux, underscoring a flux-specific influence on particle formation. Pore formation may result from a secondary phase, associated with $CaCO_3$ stabilised by Bi^{3+} and Li_2CO_3, migrating to the surface. Alternatively, it may be caused by the evaporation of lithium and other volatile species during high-temperature synthesis.

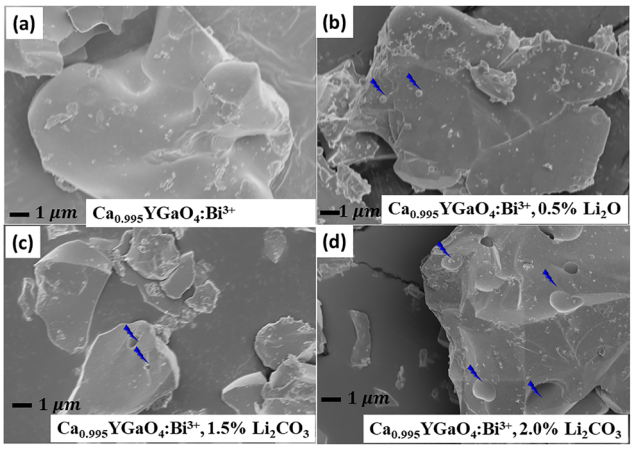

Fig. 4 SEM images of $Ca_{0.995}YGaO_4$:0.5%Bi^{3+} phosphor samples synthesised under different flux conditions: (a) without flux, (b) with Li_2O, (c) and (d) with Li_2CO_3. The blue indicators highlight soft, molten-like spherical particles and visible pores observed in the Li_2CO_3-treated samples.

3.4. XPS results of O 1s peaks

To gain deeper insight into the microstructural characteristics and chemical environment of the phosphors, high-resolution O 1s XPS measurements were carried out on three representative samples: pristine $Ca_{0.995}YGaO_4$:0.5%Bi^{3+} and samples treated with 1.5% and 2.5% Li_2CO_3 flux. The fitted O 1s spectra, shown in Fig. 5(a)–(c), reveal two distinct oxygen-related components. The dominant peak at 528–531 eV corresponds to lattice oxygen tightly bound within the crystal framework.[3] The secondary peak, centred at 531–534 eV, is typically attributed to oxygen vacancies, surface adsorbed oxygen species, or oxygen within secondary phases.[3] To quantify the relative contributions of these

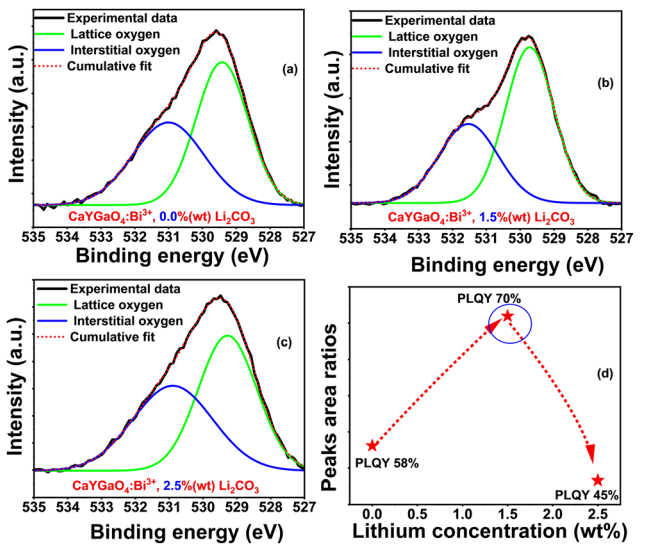

Fig. 5 High-resolution O 1s XPS spectra of $Ca_{0.995}YGaO_4$:0.5%Bi^{3+} phosphor samples synthesised under varying flux conditions: (a) without lithium flux, (b) with 1.5% Li_2CO_3, and (c) with 2.5% Li_2CO_3. Panel (d) displays the corresponding area ratios of the fitted O 1s peaks, highlighting the relative contributions of lattice oxygen and vacancy-related components.

components, Fig. 5(d) presents the area ratio, calculated using eqn (2):

$$\text{Area ratios} = \frac{\text{area}_{(528-531)\text{ eV}}}{\text{area}_{(531-534)\text{ eV}}}, \quad (2)$$

Samples exhibiting higher area ratios indicative of a lower concentration of vacancy-related oxygen species tend to demonstrate enhanced PLQY, as will be discussed in the luminescence section. This correlation underscores the critical role of oxygen-related defects in governing the optical performance of the material.

Fig. 6(a)–(c) shows the O 1s spectra of the Li_2O flux samples, and Fig. 6(d) presents the corresponding lattice to defect oxygen area ratios. The 0.5% and 1.0% Li_2O samples exhibit low ratios, indicating a high concentration of oxygen related defects. In contrast, the 1.5% Li_2O sample shows a marked increase in this ratio, reflecting a substantial reduction in defect density. This improvement is likely linked to enhanced mass transport and crystallization at higher Li_2O loading particularly as samples above 1.5% Li_2O begin to show partial melting which promotes more complete oxygen incorporation and suppresses vacancy formation. The secondary phase detected by XRD at 1.5% Li_2O may further stabilize oxygen stoichiometry.

When comparing the O 1s area-ratio trends of the Li_2O and Li_2CO_3 flux samples, the behaviour differs: low Li_2O concentrations lead to higher defect levels, whereas Li_2CO_3 at low concentration effectively suppresses defects.

At higher Li_2O loading the defect density decreases, while for Li_2CO_3 the defect-related oxygen component increases again at higher flux concentration.

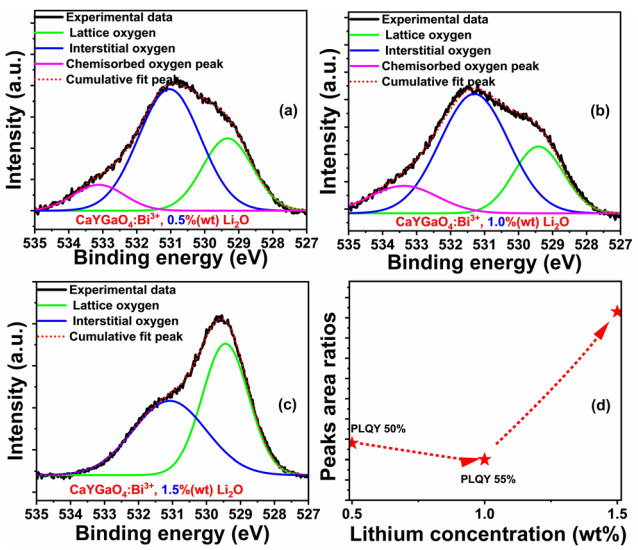

Fig. 6 High-resolution O 1s XPS spectra of $Ca_{0.995}YGaO_4$:0.5%Bi^{3+} phosphor samples synthesised under varying the Li_2O flux conditions: (a) with 0.5% Li_2O, (b) 1.0% Li_2O and (c) with 1.5% Li_2O. Panel (d) displays the corresponding area ratios of the fitted O 1s peaks, highlighting the relative contributions of lattice oxygen and vacancy-related components.

In summary, the O 1s XPS analysis demonstrates that both Li_2CO_3 and Li_2O fluxes modulate oxygen-related defects, but through distinct concentration dependent mechanisms. In the Li_2CO_3 system, defect suppression is most effective at moderate loading (1.5%), whereas higher concentrations lead to a resurgence of vacancy-related oxygen species. By contrast, the Li_2O system exhibits a high defect density at low loadings (0.5–1.0%), followed by a pronounced reduction at 1.5%, consistent with flux-mediated partial melting and enhanced mass transport that promote more complete oxygen incorporation. The observed decrease in vacancy-related oxygen components at these optimal concentrations correlates directly with the enhancement in PLQY, confirming that the suppression of non-radiative recombination centres particularly oxygen vacancies is a key mechanism by which lithium-based fluxes improve the luminescence efficiency of $CaYGaO_4:Bi^{3+}$ phosphors.

3.5. Luminescence properties

3.5.1. Origin of blue emission. The excitation and emission spectra of $Ca_{0.995}YGaO_4$:0.5%Bi^{3+} phosphor materials are given in Fig. 7(a). The observed emission band spans 350 to 550 nm, with a peak at 430 nm corresponding to the $^3P_1 \rightarrow {}^1S_0$

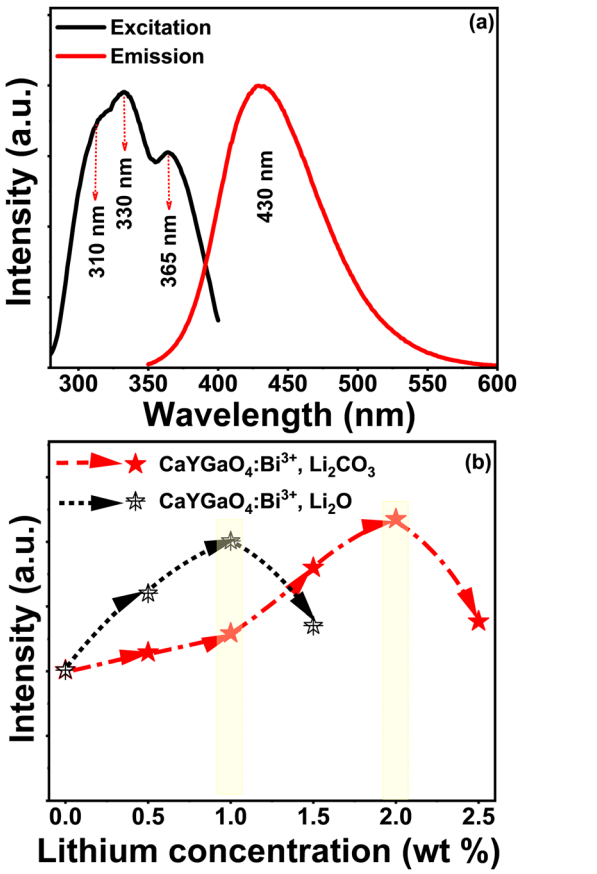

Fig. 7 (a) Excitation spectrum monitored at 430 nm and emission spectrum recorded under 330 nm excitation for $Ca_{0.995}YGaO_4$:0.5%Bi^{3+} phosphor. (b) Photoluminescence (PL) intensity as a function of lithium-based flux concentration (Li_2O and Li_2CO_3), highlighting the flux-dependent enhancement behaviour.

transition of Bi^{3+}. This electric dipole-allowed transition is commonly responsible also for blue luminescence in oxide and perovskite hosts.[2,3] Notably, the shape and position of the emission band remain unchanged upon the addition of lithium-based fluxes (Li_2O and Li_2CO_3), suggesting that the local electronic environment surrounding Bi^{3+} remains intact, even as flux treatments modulate crystallinity and emission intensity. The excitation band also plotted in Fig. 7(a) extends from 280 to 350 nm, with distinct peaks at 310, 330, and 365 nm for the pristine sample. These features are consistent with the previously reported spectral characteristics of $CaYGaO_4:Bi^{3+}$, which exhibit a broad excitation profile and an emission maximum centred at approximately 435 nm.[2,3] Further insights into these excitation features could be achieved *via* spectral fitting methods such as Gaussian fitting to resolve overlapping transitions and assign site-specific electronic origins. This analysis will be expanded upon in Section 3.5.2.

Fig. 7(b) illustrates the impact of lithium-based fluxes Li_2O and Li_2CO_3 on the blue emission intensity of $Ca_{0.995}YGaO_4:0.5\%Bi^{3+}$ phosphors under 330 nm excitation. Both fluxes enhance emission up to an optimal concentration, beyond which a decline is observed. This behaviour indicates that moderate flux concentration promotes improved crystallinity and favourable local coordination, while excessive flux leads to defect formation and emission quenching, as evidenced by the structural insights presented in Section 3.4 based on XPS analysis. The optimal enhancement concentration differs between the fluxes, reflecting distinct fluxing efficiencies and lattice interactions.

Fu *et al.*[2] reported a comparable enhancement in photoluminescence (PL) intensity with the use of Li_2CO_3 flux, demonstrating its effectiveness in boosting blue PL emission in $CaY_{0.995}GaO_4:0.5\%Bi^{3+}$ phosphors under near-UV excitation.[2] Their findings showed a ~1.5-fold increase in emission intensity over the pristine sample at optimal Li_2CO_3 content, attributed to reduced surface defects, improved crystallinity, and enhanced Bi^{3+} incorporation into the host lattice. In the present study, a distinct synthesis approach based on calcium deficiency yields a significantly greater PL enhancement. Specifically, the inclusion of 1 wt% Li_2O results in a 1.9-fold increase in emission intensity, and 2 wt% Li_2CO_3 leads to an even more notable ~2.2-fold improvement relative to the pristine sample. These results indicate a synergistic effect between Ca-deficient synthesis and lithium flux, surpassing earlier PL enhancement reports and offering a promising new strategy for optimizing Bi^{3+}-activated phosphors. This contrast highlights the varying fluxing capacities of Li_2O and Li_2CO_3, and underscores their distinct roles in modulating the luminescence properties of $Ca_{0.995}YGaO_4:0.5\%Bi^{3+}$. This enhancement is attributed to lattice modification and charge compensation, where Li^+ ions facilitate Bi^{3+} substitution at Ca^{2+} lattice sites and mitigate non-radiative recombination by correcting aliovalent charge imbalance.[29]

Lithium carbonate flux profoundly influence Bi^{3+}-doped $CaYGaO_4$ phosphors, with Li_2CO_3 enabling record-high PLQY and Li_2O promoting alternative oxide phases. These findings highlight flux chemistry as a versatile tool for engineering efficient blue emitters.

3.5.2. Fitting the excitation bands spectra. As noted earlier, the excitation profile of the flux-free sample exhibits a broad band with three distinct maxima at approximately 4.0, 3.7, and 3.4 eV (corresponding to 310, 330, and 365 nm, respectively), consistent with the excitation features reported by Fu *et al.*[2] and Wang *et al.*[3] In contrast, samples synthesized using lithium-based fluxes show clear variations in both the relative intensities of these bands (Fig. 7) and the excitation spectral shape (Fig. 8(c)–(f)). While most previous studies have focused on the emission-band shape and its correlation with dopant site occupation typically through Gaussian deconvolution, as demonstrated by Wang *et al.*[3] and Zhang *et al.*[30] the present work instead examines the excitation profile and its relationship to dopant site occupancy. This interpretation is supported by the observed changes in excitation-band shape and relative intensities, together with complementary evidence from XPS and relevant literature.

To elucidate the behaviour of the excitation bands, the normalized excitation spectra were decomposed into Gaussian components for all synthesis conditions, including the two

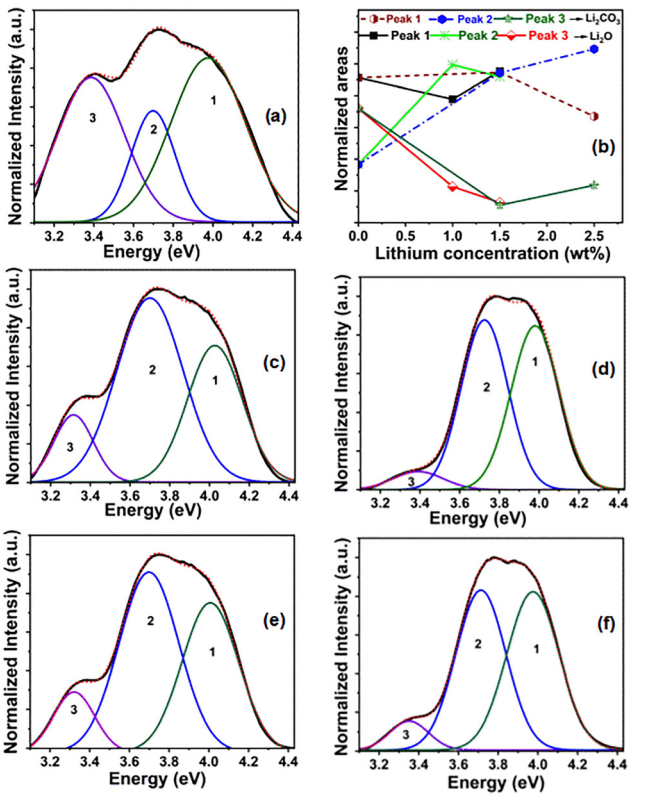

Fig. 8 (a) Gaussian peak fitting of the excitation spectrum for the flux-free sample, revealing three components: peak 1, peak 2, and peak 3. The red dotted curve represents the cumulative fit, showing close agreement with the experimental data (black). (b) Evolution of area ratios for the fitted excitation peaks in samples treated with Li_2CO_3 and Li_2O lithium-based fluxes. (c) and (d) Excitation spectra for samples treated with Li_2CO_3 at different concentrations. (e) and (f) Excitation spectra for samples treated with Li_2O at different concentrations.

lithium-based fluxes and the flux-free sample. Fig. 7(a) shows the Gaussian fitting for the flux-free sample, while Fig. 7(b) illustrates the variation in peak areas as a function of lithium-flux concentration. Fig. 8(c)–(f) display the corresponding decomposed components for the samples synthesized with lithium-based fluxes. The area of each peak was calculated and normalized to the total integrated area of all three peaks, allowing a direct comparison of the relative contributions of the deconvoluted components.

In these figures, the red dotted line represents the cumulative fit obtained from the superposition of the three Gaussian components, which closely reproduces the experimental spectrum shown in black. Based on the fitted peaks, the following assignments are proposed:

peak 1 (4.0 eV): $^1S_0 \rightarrow {}^3P_1$ transition of Bi^{3+} ions in low-symmetry environments, likely corresponding to Bi^{3+} substituting Y^{3+} sites.[2]

Peak 2 (3.7 eV): dipole-allowed $^1S_0 \rightarrow {}^3P_1$ transition associated with Bi^{3+} ions occupying Ca^{2+} lattice sites.[2]

Peak 3 (3.4 eV): excitation involving defect-related localized states near Bi^{3+} ions. This region may also overlap with Bi^{2+} excitation, as experimental result represented in Fig. 8(a), which will be discussed later.

As shown in Fig. 8(b), the flux-free sample is dominated by peaks 1 and 3, indicating that excitation primarily involves Bi^{3+} ions on Y^{3+} sites and defect-mediated localized states. Upon the introduction of Li_2CO_3 flux, the relative area of peak 1 decreases, while peak 2 becomes increasingly dominant, suggesting that Li^+ promotes the incorporation of Bi^{3+} into Ca^{2+} lattice sites where the local symmetry favors efficient dipole-allowed transitions. This behaviour is attributed to the ability of Li^+ ions to provide charge compensation, thereby reducing cation vacancies and facilitating the incorporation of additional Bi^{3+} ions into the host lattice, consistent with the findings of Wang *et al.*[3]

The area of peak 3 initially decreases, reaching a minimum at the Li_2CO_3 concentration corresponding to the highest photoluminescence (PL) intensity, indicating reduced defect-mediated excitation. At higher Li_2CO_3 concentrations, however, peak 3 increases again, implying that excess Li^+ introduces additional defects that promote non-radiative pathways or trap-state formation.

In the case of Li_2O flux, Li_2O concentrations above 1.5 wt% could not be employed due to sample melting. Within the accessible Li_2O concentration range, peak 1 shows a decreasing normalized area as Li_2O concentration increases up to 1 wt%, after which it begins to rise, indicating the Li_2O flux-induced enhancement of luminescent centers where Bi^{3+} occupies Y^{3+} lattice sites. Peak 2 exhibits a strong increase in normalized area at 1 wt% Li_2O, followed by a decrease, suggesting that Li^+ promotes the incorporation of Bi^{3+} into Ca^{2+} lattice sites at lower Li_2O concentrations compared with Li_2CO_3. The area of peak 3 shows a slight decrease with increasing Li_2O concentration, indicating a modest reduction in the defect-mediated excitation band in Li_2O samples as concentration rises.

Taken together, these trends show that the two lithium fluxes modulate Bi^{3+} site occupancy and the defect landscape in distinct ways, thereby controlling the balance between radiative and non-radiative excitation pathways. The behaviour of peak 3, associated with defect-related excitation, aligns with the XPS findings in Section 3.4. Overall, the results indicate that lithium-based fluxes tune the excitation dynamics by altering Bi^{3+} site occupancy and the local lattice environment. Gaussian deconvolution is used here only as a phenomenological aid; the mechanistic interpretation is supported by the combined evidence from PL, XPS, PLQY, and the literature rather than deconvolution alone.

3.5.3. Origin of deep-red and near-infrared emission. As reported in the literature, Bi^{2+} ions show deep-red and near-infrared (NIR) emission.[12,23,31] Accordingly, the luminescence observed in $Ca_{0.995}YGaO_4$:0.5%Bi^{3+} phosphor materials suggests that a fraction of Bi^{3+} ions undergo valence state reduction to Bi^{2+}, likely facilitated by substitution at Ca^{2+} lattice sites. The emission spectrum in Fig. 9(a) confirms that Bi^{2+} ions

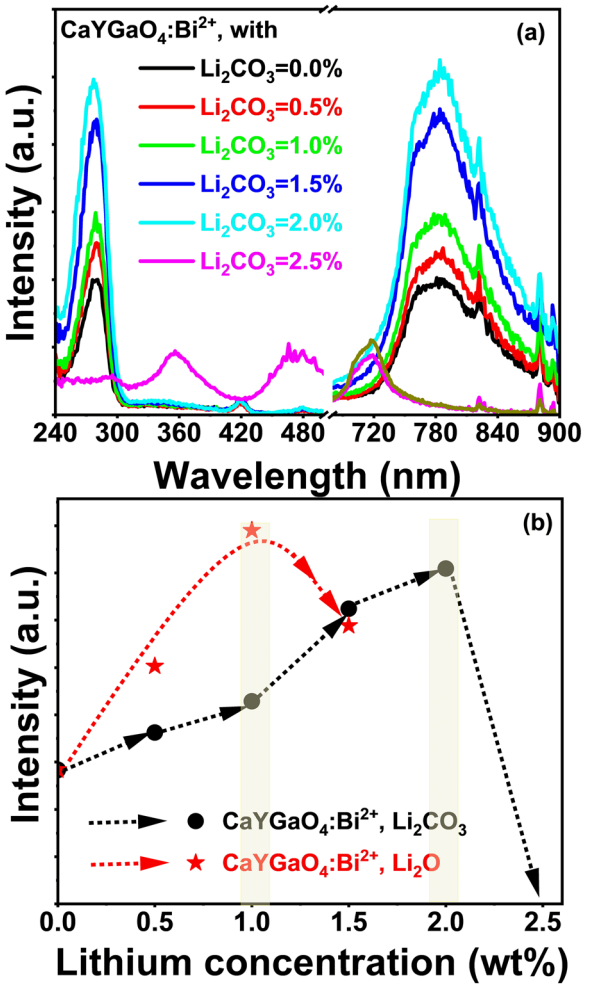

Fig. 9 (a) Shows the deep-red and NIR emission of Bi^{2+} ions in the $Ca_{0.995}YGaO_4$ phosphor host under 280 nm excitation, alongside the corresponding excitation spectra monitored at 780 nm. The second two emission bands, centred at 720 nm, appears under excitation at 360 and 480 nm; due to its weak intensity, it is scaled by a factor of 2 for visibility. (b) Relative emission intensities at 720 nm as a function of lithium-based flux concentration, recorded under an excitation wavelength of 280 nm.

reside in structurally distinct local environments. This is evidenced by two separate emission bands centred at 720 nm and 780 nm, each corresponding to Bi^{2+} ions occupying different lattice sites or coordination environments within the host matrix. The first component, a broad band centred at 780 nm under 280 nm excitation, is attributed to Bi^{2+} ions stabilised in the $Ca_{0.995}YGaO_4$ lattice through valence fluctuation disorder involving Bi^{3+}/Bi^{2+} redox pairs, as shown in Fig. 9(a). This emission feature appears consistently across all samples treated with and without lithium-based fluxes, with the exception of the specimen containing a high concentration of Li_2CO_3.

As shown in Fig. 9(b), the intensity of the 780 nm emission depends on the lithium flux content. Notably, phosphors treated with 1 wt% Li_2O and 2 wt% Li_2CO_3 exhibit enhancements of approximately 2.8-fold and 2.5-fold, respectively, compared to the pristine sample. The second component, centred at 720 nm, emerges under excitation at 360 and 480 nm, suggesting that Bi^{2+} ions in alternative coordination environments also contribute to the luminescence. This interpretation is further supported by the appearance of an additional XRD diffraction peak, tentatively attributed to a secondary phase such as $CaCO_3$:Bi^{2+},Li^+, implying partial segregation or stabilization of Bi^{2+} within a carbonate-rich environment promoted by lithium flux incorporation.

Although the emission from Bi^{2+} as a red and NIR emitter under appropriate excitation conditions has been well documented across various host matrices and excitation sources (see Table 2). However, this behaviour has not yet been reported for the $CaYGaO_4$ host.

3.5.4. Simplified energy level diagram for $Ca_{0.995}YGaO_4$:Bi^{3+},Bi^{2+} phosphor. Fig. 10 presents a simplified energy level diagram illustrating the luminescence mechanisms of $Ca_{0.995}YGaO_4$:Bi^{3+},Bi^{2+} phosphors synthesised with and without Li_2CO_3/Li_2O flux. Fig. 10(a) showcases Bi^{3+}-related blue emissions, resulting from excitation to multiple electronic states ($^3P_0$, $^3P_1$, $^3P_2$, and $^1P_1$) *via* distinct absorption bands centred around 310 nm, 330 nm, and 365 nm. These transitions correspond to peak 1, peak 2, and peak 3, as detailed in the fitted excitation band spectra in Section 3.5.2. The emissions arise from transitions originating from the $^1S_0$ ground state, reflecting the typical behaviour of Bi^{3+} in a distorted crystal field environment.[13] Fig. 10(b) and (c) illustrate Bi^{2+} emissions in the deep red and NIR regions, attributed to Bi^{2+} ions occupying two distinct lattice sites. Based on the

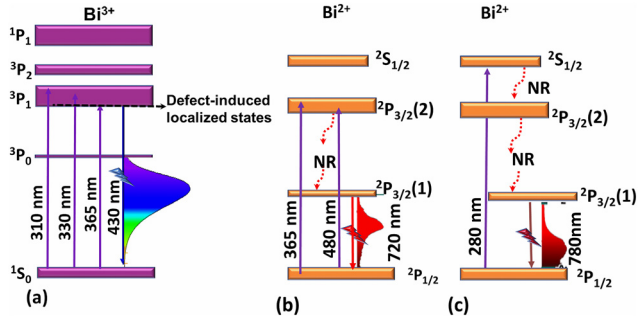

Fig. 10 Simplified energy level diagram for $Ca_{0.995}YGaO_4$:Bi^{3+},Bi^{2+} phosphors with and without Li_2CO_3/Li_2O flux. Subfigure (a) illustrates Bi^{3+}-induced blue emission *via* three excitation bands, while (b) and (c) depict Bi^{2+} emission in deep red and NIR regions, each arising from distinct local environments.

electronic configuration of Bi^{2+} [Xe]$4f^{14}5d^{10}6s^26p^1$, the following absorptive transitions are identified: (i) $^2P_{1/2} \rightarrow {}^2P_{3/2}(2)$: detected exclusively in samples synthesised under high Li_2CO_3 flux, indicating the emergence of a secondary Bi^{2+}-rich phase; (ii) $^2P_{1/2} \rightarrow {}^2S_{1/2}$: assigned to Bi^{2+} ions incorporated into the $Ca_{0.995}YGaO_4$ host lattice. Subsequent to these excitations, non-radiative relaxation occurs to the $^2P_{3/2}(1)$ level, followed by a radiative transition $^2P_{3/2}(1) \rightarrow {}^2P_{1/2}$ yielding emissions at 480 nm, 720 nm, and 780 nm. The broad emission profiles and their extension into the NIR region are attributed to wavefunction mixing, driven by local lattice distortions that perturb the Bi^{2+} energy landscape.[23,31]

3.5.5. PLQY results. Fig. 11 illustrates the PLQY of $Ca_{0.995}YGaO_4$:0.5%Bi^{3+} phosphors as a function of lithium-based flux precursors, measured under 325 nm LED excitation. Incorporation of Li_2CO_3 enhances the PLQY from 58% to 70%, whereas Li_2O reduces it to 50–55%, underscoring the pivotal role of flux chemistry in modulating luminescent performance through its influence on crystal quality and defect dynamics.

For our sample with an absorptance measured in the integrating sphere of 17%, the PLQY error was estimated following the method of Madirov *et al.*[19] For this absorbance,

Table 2 Deep-red and NIR emission of Bi^{2+} ions observed in diverse host materials

Phosphor	Centre of excitation/ emission bands (nm)	Ref.
$SrSnO_3$:Bi^{2+}	298/808	31
$SrAl_4O_7$:Bi^{2+}	280/710	23
CaO:Bi^{2+}	Electron beam/775	12
$Ca_{0.995}YGaO_4$:Bi^{2+} (low Li_2CO_3/Li_2O flux)	280/780	This work
$Ca_{0.995}YGaO_4$:Bi^{2+} (high Li_2CO_3 flux)	360 & 480/720	This work

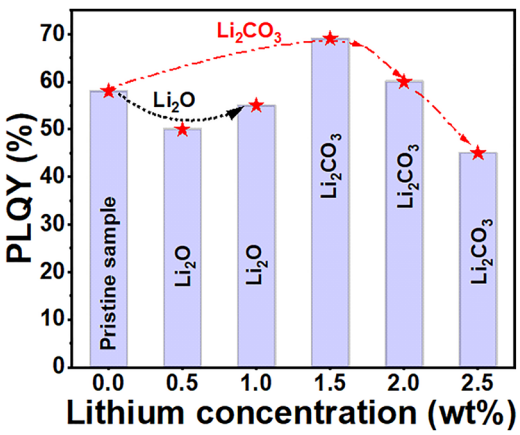

Fig. 11 PLQY of $Ca_{0.995}YGaO_4$:0.5%Bi^{3+} phosphor as a function of lithium-based flux precursors.

the relative error is expected to be ~5%, which is also consistent with relative uncertainty of 3.4% for replicated measurements reported by Bhiri *et al.* for YPO_4:Yb^{3+},Er^{3+} phosphors with a slightly higher absorptance of ~30%.[32]

The PLQY of the 2.5% Li_2CO_3 sample was measured to be 45% (Fig. 5), consistent with the earlier explanation that higher flux concentrations promote defect formation. Beyond the 1.5% level, further increases in Li_2CO_3 resulted in a progressive decline in PLQY, most likely due to the generation of additional non-radiative defects and flux-induced quenching effects. This behaviour highlights the critical importance of maintaining an optimal flux concentration to balance defect passivation with luminescence efficiency. The PLQY improvement associated with Li_2CO_3 is attributed to enhanced crystallinity and a reduced density of non-radiative defects, as confirmed by XRD and XPS analyses discussed earlier. In contrast, Li_2O appears to induce lattice distortions and promote defect states that act as quenching centres, thereby suppressing PLQY. This disparity likely arises from the higher defect concentration introduced during flux-assisted synthesis. Although direct crystallographic evidence of Bi site substitution and Bi^{2+} formation is challenging, complementary PL, XPS, and PLQY observations converge to support these mechanisms. Our results show that Li_2CO_3 uniquely suppresses oxygen defects, stabilises Bi^{3+}/Bi^{2+} coexistence, and enables dual emission, whereas Li_2O fails to achieve these effects. This establishes a previously unreported mechanistic link between flux chemistry and photophysical behaviour in $CaYGaO_4$. The beneficial role of lithium fluxes, particularly Li_2CO_3, is well supported in the literature for other host systems. Notably, Kim *et al.* demonstrated that Li_2CO_3 acts as a self-purifying flux, significantly improving crystallinity in Ba_2SiO_4:Eu^{2+} phosphors by removing impurities from low-grade starting materials.[33]

A comparative summary of PLQY values for Bi^{3+}-doped gallates is presented in Table 3, highlighting the superior performance of the current material. Reported PLQY values for Bi^{3+}-activated gallate phosphors exhibiting structural similarity to $CaYGaO_4$ including $BaLaGaO_4$, $SrLaGaO_4$, and $CaLaGaO_4$ further underscore the relevance of host lattice design. These compounds are known to exhibit blue-region luminescence, and their PLQY benchmarks provide a meaningful context for evaluating the efficiency of $CaYGaO_4$-based systems.

Table 3 Reported PLQY values for Bi^{3+}-activated layered gallate phosphors exhibiting structural similarity to $CaYGaO_4$, with a focus on compounds such as $BaLaGaO_4$, $SrLaGaO_4$, and $CaLaGaO_4$ that demonstrate blue-region luminescence

Phosphor composition	Excitation/emission (nm)	PLQY (%)	Ref.
$CaYGaO_4$:Bi^{3+}	370/470	45.7	2
$CaLaGaO_4$:Bi^{3+}	361/448	60.8	34
$SrLaGaO_4$:Bi^{3+}	320/455	50	35
$BaLaGaO_4$:Bi^{3+}	360/455	45	36
$CaYGaO_4$:Bi^{3+}	325/430	58	This work
$CaYGaO_4$:Bi^{3+}/Li_2CO_3 flux	325/430	70	This work
$CaYGaO_4$:Bi^{3+}/Li_2O flux	325/430	55	This work

4. Conclusions

$Ca_{0.995}YGaO_4$:0.5%Bi^{3+} phosphors were successfully synthesized *via* high-temperature solid-state reactions utilizing lithium-based fluxes. The resulting materials exhibited intense blue emission at 430 nm, alongside red and NIR emissions at 720 and 780 nm, which are attributed to Bi^{2+} species stabilized by lithium-induced lattice rearrangements. Comparative studies revealed that Li_2CO_3 significantly outperformed Li_2O, achieving a record-high PLQY of 70% compared to 55% for Li_2O and 58% for the flux-free sample. This enhancement is rooted in a dual mechanistic role: physically, the lithium flux promotes liquid-phase sintering and mass transport by lowering the eutectic temperature of the system; chemically, Li^+ ions act as critical charge compensators that effectively suppress non-radiative oxygen-related defects. Ultimately, these findings underscore the decisive role of flux chemistry as a versatile tool for tailoring defect environments and stabilizing mixed-valence bismuth states, providing a robust strategy for engineering next-generation, high-efficiency blue-emitting oxide phosphors.

Author contributions

Abdelrhman Yousif conducted a comprehensive evaluation of synthetic protocols from the literature, developed procedural modifications, synthesized all samples, performed X-ray diffraction and luminescence measurements, and prepared the simplified energy level diagram. Krishnan Rajagopalan performed scanning electron microscopy (SEM), conducted Rietveld refinement, and drafted the structural analysis section. E. Coetsee conducted X-ray photoelectron spectroscopy (XPS) and assisted in data analysis. Dmitry Busko measured the photoluminescence quantum yield (PLQY). Bryce S. Richards hosted the research, contributed to the conceptualization of the experiments and manuscript, and provided multiple rounds of critical proofreading, addressing both structure and language. Andrey Turshatov contributed to the conception of the experiments and manuscript, supervised the experimental work, authored substantial portions of the manuscript, performed proofreading, and managed the submission process.

Conflicts of interest

There is no conflict of interest to disclose.

Data availability

The data supporting this article have been included as part of the supplementary information (SI). Supplementary information is available. See DOI: https://doi.org/10.1039/d5tc03655k.

Acknowledgements

The financial support provided by the Helmholtz Association is gratefully acknowledged: (i) a Recruitment Initiative Fellowship

for B. S. R.; (ii) the funding of chemical synthesis equipment from the Helmholtz Materials Energy Foundry (HEMF); and (iii) Research Field Energy – Program Materials and Technologies for the Energy Transition – Topic 1 Photovoltaics (38.01.02). The first author gratefully acknowledges the financial support provided by the Philipp Schwartz Initiative (Grant No. Philipp Schwartz Initiative fellowship for A.Y.) from the Alexander-von-Humboldt Foundation for researchers at risk. Additionally, the authors sincerely thanks Dr Guojun Gao (Polysecure GmbH, Freiburg, Germany) for his valuable assistance with particle size measurements.

References

1 R. Clark, S. J. Zhu, S.-T. Zheng, X. Bu and S. Derakhshan, *J. Alloys Compd.*, 2014, **616**, 340–344.
2 Y. Fu, P. Xiong, X. Liu, X. Wang, S. Wu, Q. Liu, M. Peng and Y. Chen, *J. Mater. Chem. C*, 2021, **9**, 303–312.
3 C. Wang, Z. Yao, Y. Lei, K. Wu, W. Dai and M. Xu, *Inorg. Chem.*, 2024, **63**, 16056–16069.
4 C. Yang, W. Liu, Q. You, X. Zhao, S. Liu, L. Xue, J. Sun and X. Jiang, *Nanomaterials*, 2023, **13**, 1715.
5 G. Huang, E. Gage, B. Breiner, M. Saavedra, D. Busko, N. J. Janowicz, D. S. Wright and B. S. Richards, *Energy Environ. Sci.*, 2025, **18**, 9435–9445.
6 B.-S. Wu, P. W. Addo, S. Macpherson, V. Orsat and M. Lefsrud, *J. Photochem. Photobiol., B*, 2025, **262**, 113069.
7 R. Müller, B. Okokhere-Edeghoghon, N. J. Janowicz, A. D. Bond, G. Kociok-Kohn, L. M. R. Cox, D. Garzon, T. W. Waine, I. G. Truckell and E. Gage, *Adv. Mater. Technol.*, 2025, **10**, 2400977.
8 K. T. Thu, N. Tu, N. Van Du, N. Van Quang, T. N. Bach, N. T. H. Lien, N. D. Hung, D. X. Viet, P. T. L. Huong and T. T. H. Tam, *RSC Adv.*, 2025, **15**, 27334–27344.
9 W. Xia, Y. Ye, Q. Mao, Y. Ding, X. Li, M. Liu and J. Zhong, *Mater. Today Chem.*, 2024, **36**, 101958.
10 J. A. do Nascimento Neto, A. K. S. M. Valdo, C. C. da Silva, F. F. Guimarães, L. H. K. Queiroz Júnior, L. J. Q. Maia, R. C. de Santana and F. T. Martins, *J. Am. Chem. Soc.*, 2019, **141**, 3400–3403.
11 L. R. Wilson and B. S. Richards, *Appl. Opt.*, 2009, **48**, 212–220.
12 A. Yousif, R. Jafer, S. Som, M. Duvenhage, E. Coetsee and H. Swart, *RSC Adv.*, 2015, **5**, 54115–54122.
13 M. Back, J. Ueda, J. Xu, K. Asami, L. Amidani, E. Trave and S. Tanabe, *J. Phys. Chem. C*, 2019, **123**, 14677–14688.
14 H. Guo, Y. Chen, S. Gu, L. Wang, Q. Shi, L. Zhao, C. E. Cui, Y. Cui and P. Huang, *J. Lumin.*, 2023, **255**, 119602.
15 Y. Chen, H. Zhang, K. Liu, X. Zhu and H. Yuan, *J. Alloys Compd.*, 2022, **918**, 165759.
16 F. Chi, Q. Liu, J. Zhang, B. Jiang, X. Niu and S. Liu, *Opt. Mater.*, 2023, **143**, 114245.
17 S. Tamura, K. Koyabu, T. Masui and N. Imanaka, *Chem. Lett.*, 2004, **33**, 58–59.
18 S. Limbu, L. R. Singh and G. S. Okram, *RSC Adv.*, 2020, **10**, 35619–35635.
19 E. Madirov, D. Busko, F. A. Cardona, D. Hudry, S. V. Kuznetsov, V. A. Konyushkin, A. N. Nakladov, A. A. Alexandrov, I. A. Howard and B. S. Richards, *Adv. Photonics Res.*, 2023, **4**, 2200187.
20 J. C. de Mello, H. F. Wittmann and R. H. Friend, *Adv. Mater.*, 1997, **9**, 230–232.
21 B. Lou, J. Wen, J. Cai, Y.-Y. Yeung, M. Yin and C.-K. Duan, *Phys. Rev. B*, 2021, **103**, 075109.
22 R. t Shannon and C. Prewitt, *Struct. Sci.*, 1970, **26**, 1046–1048.
23 M. Puchalska, P. Bolek, K. Kot and E. Zych, *Opt. Mater.*, 2020, **107**, 109999.
24 K. Ogawa, R. Abe and A. Walsh, *J. Am. Chem. Soc.*, 2024, **146**, 5806–5810.
25 B. Ahmed, S. R. Devi and B. I. Sharma, *Interactions*, 2024, **246**, 8.
26 P. Singh, P. Maneesha, M. Kumari, A. Mekki, K. Harrabi and S. Sen, *J. Electroanal. Chem.*, 2026, **2026**, 119883.
27 F. Kang, J. Han and M. Peng, *Chin. J. Appl. Chem.*, 2016, **33**, 1420–1427.
28 P. Han, X. Jiang, L. Zhang, F. Yu, Q. Shi, Y. Ding and Q. Zhang, *J. Mater. Sci.: Mater. Electron.*, 2015, **26**, 666–670.
29 P. Dang, S. Liang, G. Li, Y. Wei, Z. Cheng, H. Lian, M. Shang, S. J. Ho and J. Lin, *J. Mater. Chem. C*, 2018, **6**, 6449–6459.
30 S. Zhang, J. Zhou, M. Wang, D. Wu and R. Zhang, *Appl. Phys. A: Mater. Sci. Process.*, 2023, **129**, 847.
31 X. Qin, Y. Li, D. Wu, Y. Wu, R. Chen, Z. Ma, S. Liu and J. Qiu, *RSC Adv.*, 2015, **5**, 101347.
32 N. M. Bhiri, H. Duim, E. Madirov, J. Nyarige, B. S. Richards and A. Turshatov, *J. Mater. Chem. C*, 2025, **13**, 4605–4615.
33 D. Kim, K.-W. Jeon, J. S. Jin, S.-G. Kang, D.-K. Seo and J.-C. Park, *RSC Adv.*, 2015, **5**, 105339.
34 C. Zuo, R. Chen, X. Jiang, Y. Yang, C. Li, C. Li, W. Yang, H. Lin, L. Liu and S. Li, *Ceram. Int.*, 2024, **50**, 29580–29589.
35 H. Yuan, H. Ma, G. Wang, H. Jia and X. Sun, *J. Mol. Struct.*, 2025, **1321**, 139776.
36 Y. Li, S. Liu, Y. Wang, K. Yan, Y. Du, Y. Hao and G. Liu, *Mater. Today Chem.*, 2025, **45**, 102652.